

## Article

# Robust Current Control of a Small-Scale Wind–Photovoltaic Hybrid System Based on the Multiport DC Converter

Farouk Mechnane <sup>1</sup>, Said Drid <sup>1,2,\*</sup>, Nasreddine Nait-Said <sup>1</sup> and Larbi Chrifi-Alaoui <sup>3</sup>

<sup>1</sup> LSP-IE Laboratory, Electrical Engineering Department, University of Batna 2, Avenue Mohamed Boukhlouf, Batna 05000, Algeria; f.mechnane@univ-batna2.dz (F.M.); n.naitsaid@univ-batna2.dz (N.N.-S.)

<sup>2</sup> Higher National School of Renewable Energy, Environment and Sustainable Development, Constantine Road, Fesdis 05078, Algeria

<sup>3</sup> LTI (UR-UPJV-3899), University of Picardie Jules Verne, 80000 Amiens, France; larbi.alaoui@u-picardie.fr

\* Correspondence: s.drid@univ-batna2.dz or s\_drid@yahoo.fr

**Abstract:** In this paper, a robust current control of the hybrid renewable energy system (HRES), based on the PV-Wind system, is proposed. The HRES is connected to a multiport converter to synchronize the multi-source system with one DC-Bus. Due to their ability to integrate many renewable energy sources (RES) individually or simultaneously, multiport converters (MPC) are an innovative method suitable for renewable energy applications. Recently, many DC-DC converter designs and topologies have emerged to ensure the highest possible efficiency of hybrid RESs. The multiport converter is a typical coupling system with several modes of operation. Thus, the design of its controller become complicated. To stabilize the DC-Bus voltage, a battery has been added to the system. In this HRES configuration, all sources are connected in parallel via the multiport DC converter. We used the multiport DC converter to minimize the intermittent character of solar and wind and control the energy flow between the different power sources and the load, as well as to increase the performance of the system. The nonlinear robust control structure is based on Lyapunov approach to overcome the nonlinear model of the system to improve robustness and guarantees the asymptotic stability. The proposed control law is implemented and tested on dSPACE-DS1104. The results show the effectiveness and the feasibility of the proposed controller.

**Keywords:** wind energy conversion system; photovoltaic system; hybrid system; robust multiport converter; MPPT; wind turbine; PMSG



**Citation:** Mechnane, F.; Drid, S.; Nait-Said, N.; Chrifi-Alaoui, L. Robust Current Control of a Small-Scale Wind–Photovoltaic Hybrid System Based on the Multiport DC Converter. *Appl. Sci.* **2023**, *13*, 7047. <https://doi.org/10.3390/app13127047>

Academic Editors: Levon Gevorgov and Olena Rubanenko

Received: 19 May 2023

Revised: 5 June 2023

Accepted: 9 June 2023

Published: 12 June 2023



**Copyright:** © 2023 by the authors. Licensee MDPI, Basel, Switzerland. This article is an open access article distributed under the terms and conditions of the Creative Commons Attribution (CC BY) license (<https://creativecommons.org/licenses/by/4.0/>).

## 1. Introduction

Due to the increasing demand for energy and according to the environmental, economic and political problems related to the use of fossil energy resources, renewable energy sources are becoming an unavoidable alternative for energy production [1]. Today, renewable energy sources have many advantages, including sustainability and low pollution. Wind and photovoltaic technologies are two examples of renewable energy systems that have the potential to replace conventional energy [2–5].

On the other hand, due to recent price drops of solar panels, it is currently estimated that installed photovoltaic capacity is expected to be equivalent to 800 GW by 2030 [6]. Experts have predicted that by 2050, wind and PV will account for about 50% of all electricity generated in the world [7,8]. Moreover, one of the main problems with these two sources is their random and intermittent nature, which makes it difficult to control their individual uses.

Therefore, the simplest solution is the hybridization of these two sources associated with a storage system. These systems have recently attracted the interest of many researchers who are working in the fields of renewable energy sources [9,10]. Three topologies of hybrids systems have been proposed: common DC-BUS, common AC-BUS and

combined common AC/DC-Bus [11]. In general, these topologies require the use of a number of power converters to adapt and facilitate the transition of energy generated from renewable sources to the final use, which adds to the system's total complexity.

Furthermore, as the numbers of converters increase, the efficiency of the system decreases due to losses in each converter [12]. The efficient control of the converters with a constant and optimal switching frequency makes it possible to minimize the heating of power components [13].

The first converters integrated in renewable energy systems were equipped with transformers to increase the generated voltages and bring them back to the same level as the grid. These topologies are known as isolated converters [14,15]. The use of transformers increases the cost and size of the installation, and the overall efficiency of such a converter is reduced [16,17].

The emergence of non-isolated converters has significantly improved the efficiency and reduced the size of the systems [18]. Generally, renewable energy systems require the use of multiple converters, which decreases the reliability of the system and increases the complexity of control. Now, many scientists are looking at the use of multiport converters (MPC) as a solution to these problem [19–21].

In fact, these converters' benefits include their centralized control, low cost, high conversion ratio, continuous input current and compact architectures [22]. In the literature, systematic approaches to the synthesis of MCs' diverse topologies based on various input sources have been also developed [23,24]. In order to allow power to flow between each port, the multiport converter's main objective is to connect several power sources with inputs and outputs through a single power converter. The redundant and unnecessary power conversion stages and excessive solid-state switching components that are frequently seen in conventional topologies are eliminated by these multiport converters [25].

Numerous recent articles have been written about various features of new multiport converter technology. The authors in [26] explained more than thirty topologies and approved the use of wide-bandgap semiconductors in each. Multiport switching zero-current converters are used in a new way for energy storage management, as described in [27]. The article in [28] provides an overview of recent advances in multiport DC-DC converters that utilize hybrid renewable power sources (HRES) for a variety of applications. In the article in [29], many single-stage multiport topologies are illustrated. Thus, multiport converters have improved the operation of these converters by integrating the system into a compact structure [30], which reduces the cost and protection equipment and facilitates the control scheme of the converter [31].

Due to fluctuations in the generated voltages, a control scheme is necessary to stabilize the output voltage level. In this context, the proposed multiport converter supports a battery port, with a bidirectional power flow [32]. The control scheme ensures the stability of the DC-Bus voltage and the extraction of the maximum power from the renewable sources [31,33–35].

In this paper, the structure of our system is presented in Figure 1. In this figure, there are two energy sources, a battery, a multiport DC converter, a DC-AC converter and loads.

The main goal of this study is the design of a robust current control of multiport DC converters. Additionally, we have applied maximum power point tracking strategies for PV and wind sources to ensure the optimum operation of our system [36–39]. The design control law is based on the Lyapunov approach. The control scheme is successfully tested using the dSPACE1104 system.

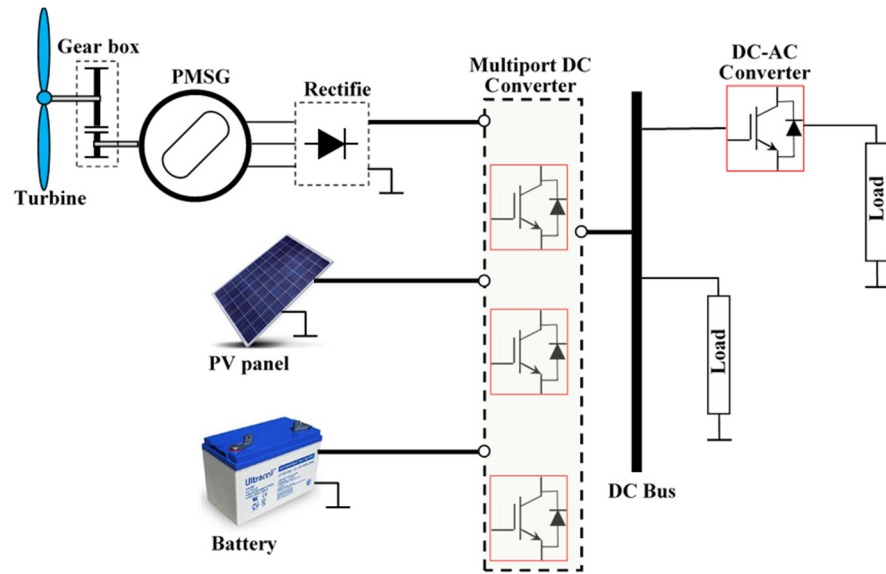


Figure 1. Schematic of the control strategy for Wind-PV system using MISO converter.

## 2. Hybrid Wind-PV System Modeling

In this work, we will focus on the study of the multipoint converter shown in Figure 1. The mathematical modeling of the proposed system is presented as follows:

### 2.1. Wind Turbine System Modeling

This part of the wind system is made up of a horizontal axis turbine, a permanent magnet generator and a diode rectifier (Figure 2). Its model is given as follows:

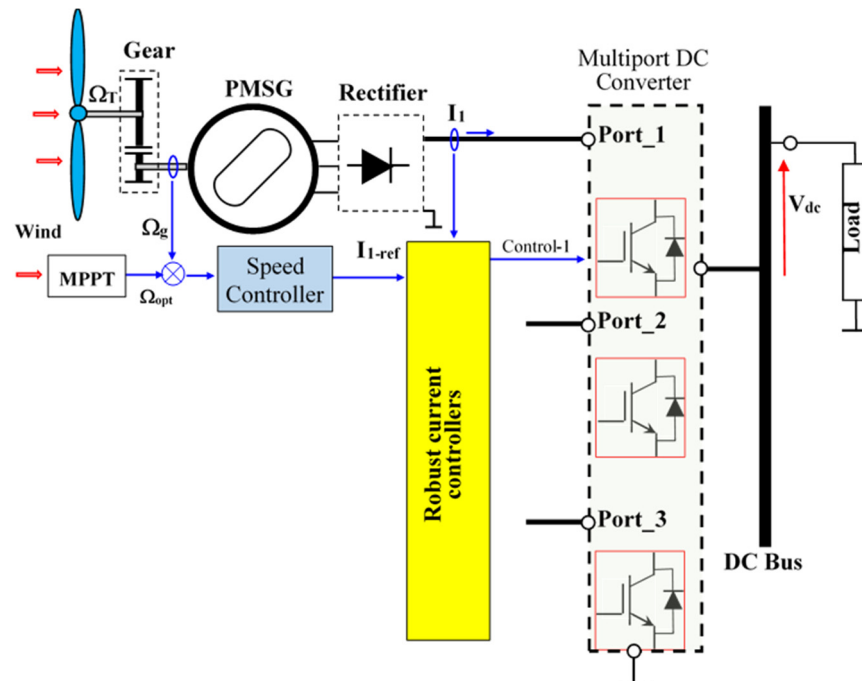


Figure 2. The wind system.

#### 2.1.1. Turbine Model

The turbine's aerodynamic power is expressed by Equation (1).

$$P_T = \frac{1}{2} \cdot \rho \cdot A \cdot v^3 \cdot C_p(\lambda, \beta), \quad (1)$$

where  $P_T$  is the turbine aerodynamic power (W),  $\rho$  is the air density ( $\text{kg/m}^3$ ),  $A$  is the area swept by the rotor blades ( $\text{m}^2$ ),  $v$  is the wind speed (m/s),  $C_p$  is power coefficient,  $\beta$  is the pitch angle (rd) and  $\lambda$  is the Tip-Speed Ratio (TSR).

The TSR is the ratio of the linear speed of the blades to wind speed, and it is represented by Equation (2).

$$\lambda = \frac{\Omega_g R}{v}, \tag{2}$$

The gear box is used between the turbine and generator in order to amplify the rotation speed. Its equation is given by Equation (3).

$$G = \frac{\Omega_g}{\Omega_T} = \frac{T_T}{T_m}, \tag{3}$$

In the literature, several equations are available to evaluate the  $C_p$ . In our case, we assume that the angle  $\beta = 0$  and the  $C_p$  is given by the following equation:

$$C_p = -0.7317\lambda^3 + 0.2953\lambda^2 + 0.8760\lambda, \tag{4}$$

The mechanical equation is expressed as

$$\frac{d\Omega}{dt} = -\frac{1}{J}(T_m - |T_{em}| - f.\Omega), \tag{5}$$

where  $T_{em}$  is the torque of the generator.

Figure 3 presents the interconnection between the scheme of Equations (1)–(5).

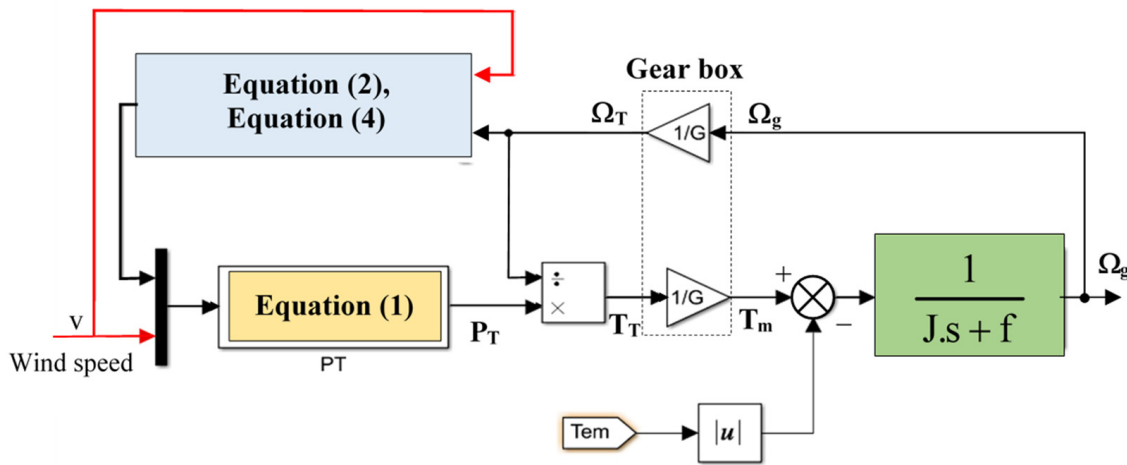


Figure 3. Turbine model scheme.

### 2.1.2. PMSG Modeling

The wind turbine based on PMSG was chosen in this work due its high efficiency and high torque development. The induced voltage magnitude and frequency of the PMSG varies with wind speed and the generated power will be converted to DC power using a rectifier in order to overcomes this issue [40]. The PMSG mathematical equations is given in synchronous frame by Equation (6) as follows:

$$\begin{cases} V_d = -R_s I_d - L_d \frac{dI_d}{dt} + L_q \omega I_q \\ V_q = -R_s I_q - L_q \frac{dI_q}{dt} - L_d \omega I_d + \phi_f \omega \\ T_{em} = -\frac{3}{2} p \phi_f I_q \end{cases}, \tag{6}$$

where  $R_s$  is the stator resistance,  $\omega$  is the rotor electric speed ( $\omega = p\Omega$ ),  $I_d$ ,  $I_q$ ,  $V_d$ ,  $V_q$ ,  $L_d$ ,  $L_q$  are, respectively, the direct and the quadrature axes components of current, voltage and stator inductance and  $\phi_f$  is the flux of the permanent magnet.

### 2.1.3. Wind MPPT Controller

In the literature, we found many MPPT techniques for wind turbine systems. In this work, we used only the Tip-Speed Ratio control which is presented in Figure 4. The optimal speed is calculated from the optimal Tip-Speed Ratio  $\lambda_{opt}$  and wind speed, as shown in Equation (7).

$$\Omega_{opt} = \frac{\lambda_{opt}G}{R} \cdot v, \tag{7}$$

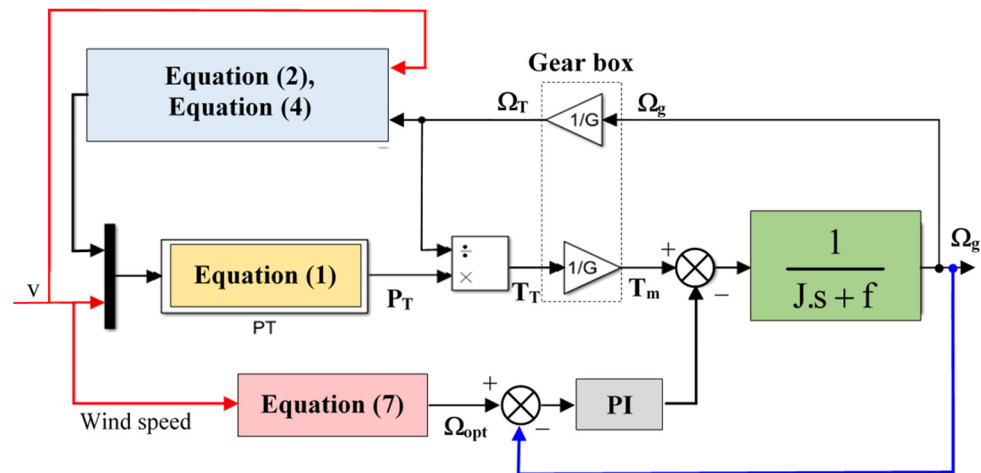


Figure 4. Principle of Tip-Speed Ratio control.

The data of the wind system panel are given in Table 1.

Table 1. Wind system data.

Description	Value
Radius R	0.62 m
Air density	1.25 kg/m <sup>3</sup>
Gear ratio G	20 A
Flux of permanent magnet	0.06 Web
Stator inductances $L_d = L_q$	10 mH
Stator resistance $R_s$	0.0675 $\Omega$
Pole numbers p	3
Total inertia, J	0.00176 kg.m <sup>2</sup>
Friction coefficient	$0.38 \times 10^{-4}$ (SI)
Optimal Tip-Speed Ratio	0.78
Maximal power coefficient $C_{pmax}$	0.515

### 2.2. PV System Modeling

The PV energy is generated from the solar irradiation using semiconductor materials (Figure 5).

### 2.3. PV Panels Model

A large number of models for describing the behavior of the solar photovoltaic panels can be found in the literature [41,42]. The most popular is the model with one diode shown in Figure 6.

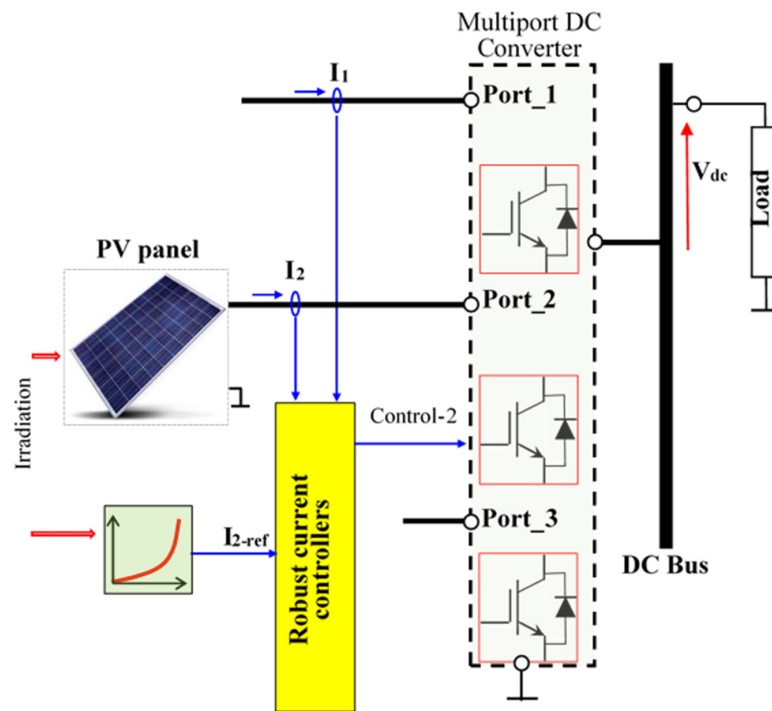


Figure 5. Model of a PV cell with one diode.

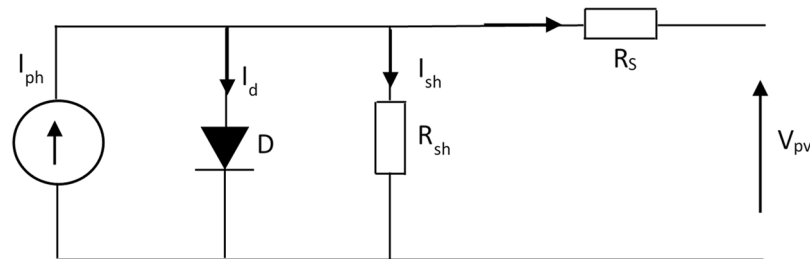


Figure 6. Model of a PV cell with one diode.

Here,  $I_{sat}$ : reverse saturation current,  $K$ : Boltzmann’s constant,  $T$ : temperature,  $e$ : electron charge,  $n$ : ideality factor,  $R_s$ : series resistor,  $R_{sh}$ : parallel resistor,  $I_{ph}$ : photonic current,  $V_{pv}$ : PV voltage and  $I_{pv}$ : PV current.

Considering a PV panel made up of  $N_p$  parallel cell strings formed of  $N_s$  cells in series and that  $R_{sh}$  is infinite, the PV model is given by Equation (8).

$$I_{pv} = N_p I_{ph} - N_p I_{sat} \exp \left( \frac{e(V_{pv} + (I_{pv} \frac{N_p}{N_s} R_s))}{nKT} - 1 \right), \tag{8}$$

The data of the used panel are given in Table 2.

Table 2. PV Panel Data.

Description	Value
Maximum power	105 W
Voltage at p max ( $V_{mp}$ )	24 V
Current at p max ( $I_{mp}$ )	4.4 A
Open-circuit voltage ( $V_{oc}$ )	32 V
Short-circuit current ( $I_{sc}$ )	5 A

The voltage–current (V-I) and voltage–power (V-P) characteristics according Equation (8) are given in Figure 7.

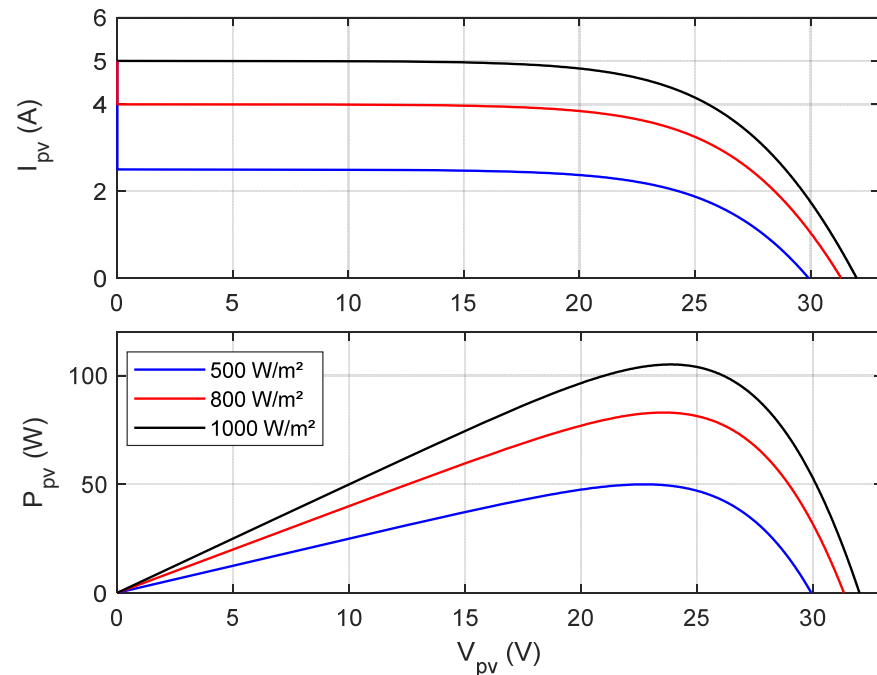


Figure 7. V-I and V-P characteristics of PV panel.

#### PV MPPT Controller

The MPPT method that we used in our work is the look-up table-based MPPT due to its simplicity and our objective being the control of the multiport DC converter. Figure 8 represents the optimal PV current according to the irradiancies.

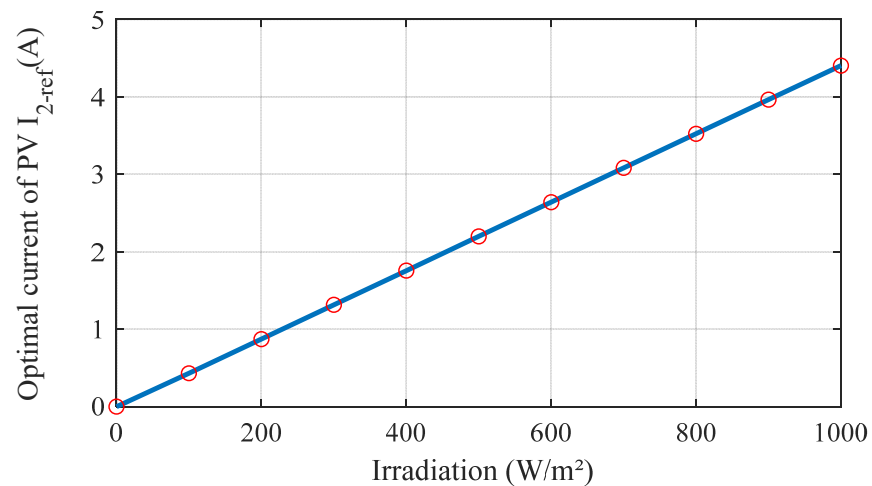


Figure 8. Look-up table of PV optimal current versus irradiancies.

#### 2.4. Battery Storage System

The battery is a very important device in the hybrid system because the system relies on its energy balance. Additionally, the battery plays a key role in the stabilization of the DC-bus voltage (Figure 9).



This converter has three input ports and one output port (Figure 10).

2.5.1. Port 1 and Port 2 Model

Port 1 and the port 2 are connected to two boost converter branches. They are used to control the current of wind system and PV system, respectively. Using the Kirchhoff law, we can rewrite average model as follows (Equation (9)):

$$\begin{cases} \frac{di_2}{dt} = \frac{V_2}{L_2} - \frac{V_{dc}}{L_2}(1 - \alpha_1) \\ \frac{di_1}{dt} = \frac{V_1}{L_1} - \frac{V_{dc}}{L_1}(1 - \alpha_2) \end{cases} \quad (9)$$

where  $\alpha_1$  and  $\alpha_2$  represent the duty cycles.

2.5.2. Port 3 Model

Port 3 is connected to the battery. It represents a bidirectional converter. We can identify two modes:

1. **Boost mode** ( $0 < \alpha < 0.5$ ): In this case, switch T3 is turned off and the control is performed only by switch T4 (Figure 11).

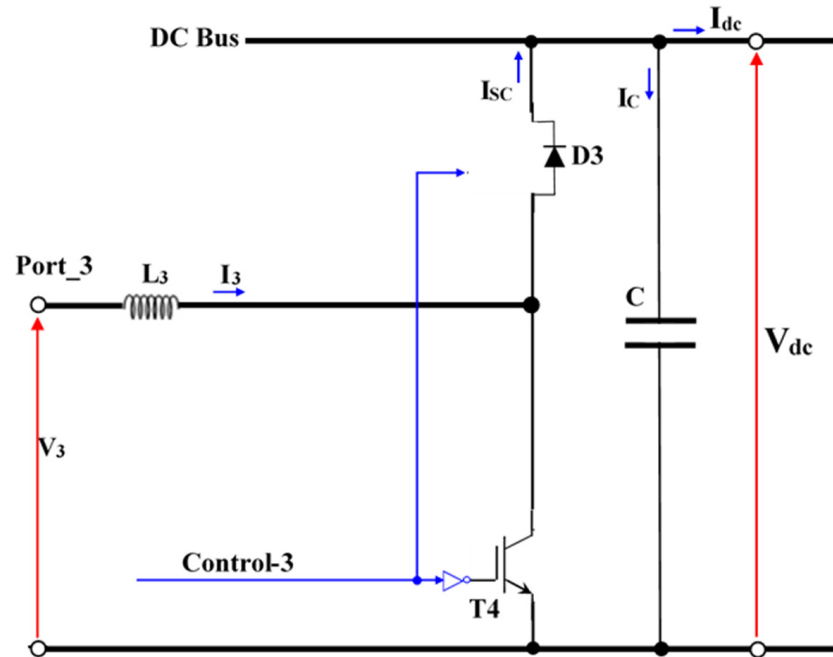


Figure 11. Boost mode.

The average model of this mode is given by Equation (10).

$$\dot{I}_3 = \frac{V_3}{L_3} - \frac{V_{dc}}{L_3}(1 - \alpha_3), \quad (10)$$

where  $\alpha_3$  represents the duty cycle. Equation (10) can be rewritten as follows:

$$\dot{I}_3 = \frac{V_3}{L_3} - \frac{V_{dc}}{L_3} + \frac{V_{dc}}{L_3}\alpha_3, \quad (11)$$

2. **Buck mode** ( $0.5 < \alpha < 1$ ): In this case, switch T4 is turned off and the control is performed only by switch T3 (Figure 12).

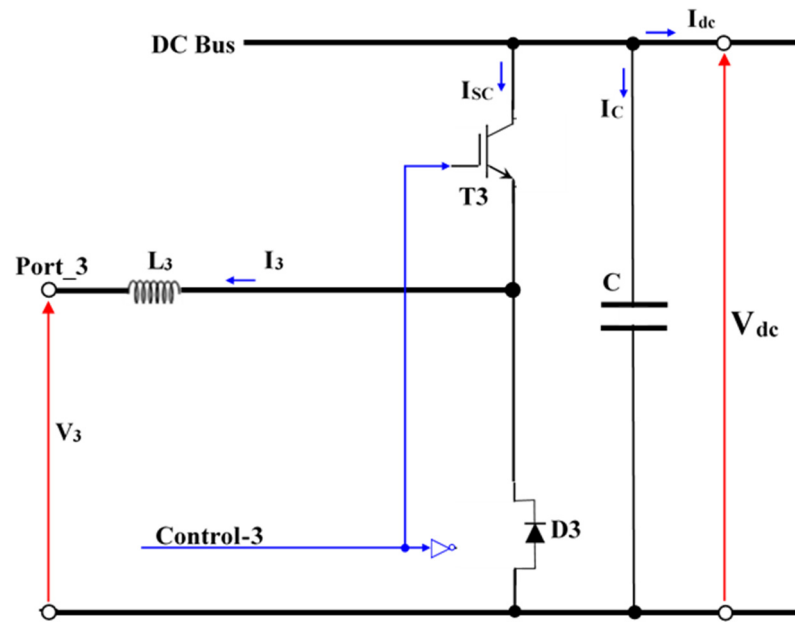


Figure 12. Buck mode.

The average model of this mode is given by Equation (12).

$$\dot{I}_3 = -\frac{V_3}{L_3} + \frac{V_{dc}}{L_3} \alpha_3, \tag{12}$$

The average model of the bidirectional branch is obtained by using the superposition principle.

According to Equations (11) and (12), we can define the following equation

$$\dot{I}_3 = \frac{V_3}{L_3} \delta_1 - \frac{V_{dc}}{L_3} \delta_2 + \frac{V_{dc}}{L_3} \alpha_3, \tag{13}$$

where

$$\delta_1 = -\text{sgn}\left(\alpha_3 - \frac{1}{2}\right) : \begin{cases} +1 & \text{if } (0 < \alpha_3 < 0.5) \\ -1 & \text{if } (0.5 < \alpha_3 < 1) \end{cases}, \tag{14}$$

and

$$\delta_2 = \frac{1}{2}(1 + \delta_1) : \begin{cases} +1 & \text{if } (0 < \alpha_3 < 0.5) \\ 0 & \text{if } (0.5 < \alpha_3 < 1) \end{cases}, \tag{15}$$

The values of  $\delta_1$  and  $\delta_2$  in Equations (14) and (15) define the mode of the bidirectional branch.

### 2.5.3. Output Model

Referring to Figure 10, the output currents and voltage can be written as follows:

$$\begin{aligned} I_{rew} &= I_{wc} + I_{pvc} \\ I_{dc} &= I_C + I_{sc} + I_{rew}, \\ I_C &= C \cdot \frac{dV_{dc}}{dt} \end{aligned} \tag{16}$$

where  $I_{sc}$  is the storage current,  $I_{wc}$  is the output wind current,  $I_{pvc}$  is the output PV current and  $I_{rew}$  is the renewable current.

In steady state, the relationship of the storage current  $I_{sc}$  and the battery current  $I_3$  is given by Equation (17)

$$I_{sc} = k_{sc} I_3, \tag{17}$$

where  $k_{sc} = 1$  for buck mode and  $k_{sc} = (1 - \alpha_3)$  for boost mode.

### 2.5.4. Stabilization of DC Voltage Output

Using Equation (16), we can design the voltage controller (Figure 13).

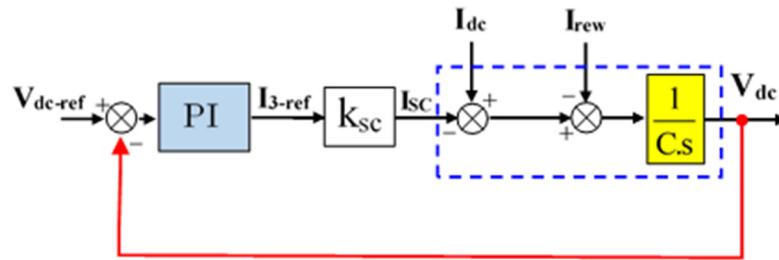


Figure 13. Output DC voltage stabilization scheme.

### 3. Robust Current Control Design Based on Lyapunov Approach

To improve the preferences of the control, robust current control based on the Lyapunov theory is applied [43]. The main objective is to achieve the optimum current control.

In steady state, the average model of the multiport DC converter can be written in continuous conduction mode by Equation (18) resulting from the combination of Equations (9) and (13).

$$\begin{cases} \dot{x}_1 = a_1 V_1 - a_1 x_4 u_1 \\ \dot{x}_2 = a_2 V_2 - a_2 x_4 u_2 \\ \dot{x}_3 = a_3 V_3 - a_{31} x_4 + a_{32} x_4 u_3 \end{cases}, \tag{18}$$

where  $u_1 = (1 - \alpha_1)$ ,  $u_2 = (1 - \alpha_2)$  and  $u_3 = \alpha_3$ ,  $a_1 = \delta_1/L_1$ ,  $a_2 = 1/L_1$ ,  $a_3 = \delta_1/L_3$ ,  $a_{31} = \delta_2/L_3$ ,  $a_{32} = 1/L_3$  and  $[x_1 \ x_2 \ x_3 \ x_4]^T = [I_1 \ I_2 \ I_3 \ V_{dc}]^T$ .

We can state the following result:

**Proposition.** Consider the state model (4). Then, the PV current, wind current and the output DC voltage reach their optimal values provided that the following control laws are used (Equation (19)).

$$\begin{cases} u_1 = \frac{1}{a_1 x_4} (a_1 V_1 - \dot{x}_1^* + K_1 e_1 + K_{11} \text{sgn}(e_1)) \\ u_2 = \frac{1}{a_2 x_4} (a_2 V_2 - \dot{x}_2^* + K_2 e_2 + K_{22} \text{sgn}(e_2)) \\ u_3 = \frac{1}{a_{32} x_4} (a_3 V_3 - \dot{x}_3^* + a_{31} x_4 + K_3 e_3 + K_{33} \text{sgn}(e_3)) \end{cases}, \tag{19}$$

where  $(K_1, K_{11}, K_2, K_{22}) > 0$ .

**Proof of Proposition.** Let the Lyapunov function related to the currentux dynamics be defined by the following equation:

$$F = \frac{1}{2} e_1^2 + \frac{1}{2} e_2^2 + \frac{1}{2} e_3^2 > 0, \tag{20}$$

where

$$\begin{cases} e_1 = (x_1 - x_1^*) \\ e_2 = (x_2 - x_2^*) \\ e_3 = (x_3 - x_3^*) \end{cases}, \tag{21}$$

The derivative of the Lyapunov function (20) becomes

$$\dot{F} = \dot{e}_1 e_1 + \dot{e}_2 e_2 + \dot{e}_3 e_3, \tag{22}$$

When (19) is substituted for (21), we obtain

$$\begin{cases} \dot{e}_1 = (\dot{x}_1 - \dot{x}_1^*) = -K_1 e_1 - K_{11} \text{sgn}(e_1) \\ \dot{e}_2 = (\dot{x}_2 - \dot{x}_2^*) = -K_2 e_2 - K_{22} \text{sgn}(e_2) \\ \dot{e}_3 = (\dot{x}_3 - \dot{x}_3^*) = -K_3 e_3 - K_{33} \text{sgn}(e_3) \end{cases} \tag{23}$$

Hence, (23) replaced in (22) gives

$$\dot{F} = -K_1e_1^2 - K_{11}e_1\text{sgn}(e_1) - K_2e_2^2 - K_{22}e_2\text{sgn}(e_2) - K_3e_3^2 - K_{33}e_3\text{sgn}(e_3) < 0, \quad (24)$$

We note that (24) is negative  $\forall(e_1, e_2, e_3, e_4)$ , thus the system is stable.  $\square$

Figure 14 presents the overall proposed scheme control.

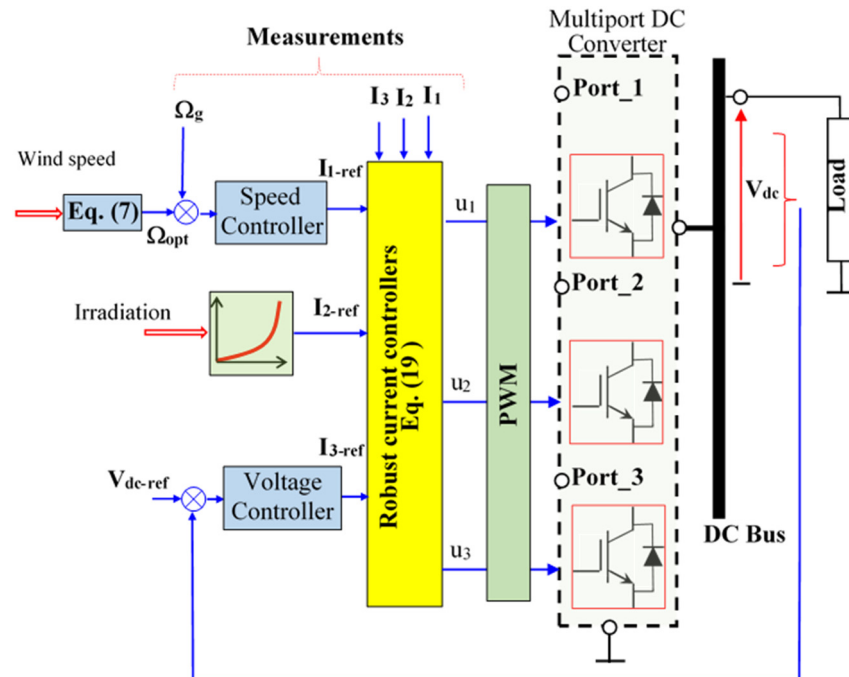


Figure 14. Proposed scheme control.

#### 4. Experimental Implementation

To test the effectiveness of the proposed control scheme, an experimental study was carried out in a laboratory setup based on dSPACE DS1104 hosted on a PC (Figure 15).

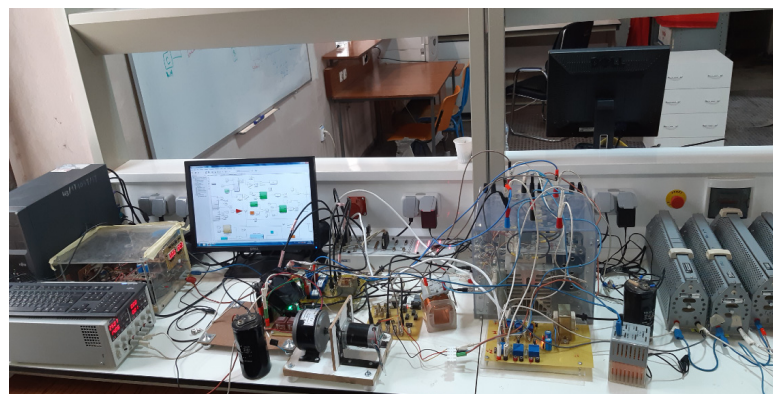


Figure 15. View of the laboratory experimental setup.

The basic structure of the laboratory setup is depicted in Figure 16. The DC motor was used to emulate the wind turbine emulator and a linear amplifier to emulate the PV panel controlled through dSPACE DS1104. The encoder was used to measure the motor speed (encoder resolution was 1024 pulses per revolution). The sensors used for measurement of currents and voltages were, respectively, LA-55NP and LV-25P. The interface was used to provide galvanic isolation to all signals connected to the DS1104 PPC controller. Addition-

ally, two lithium iron phosphate batteries (LifeP04) were used. All sources were connected to SEMIKRON with IGBT power moduli SKM50GB123 and SKM50GAL123.

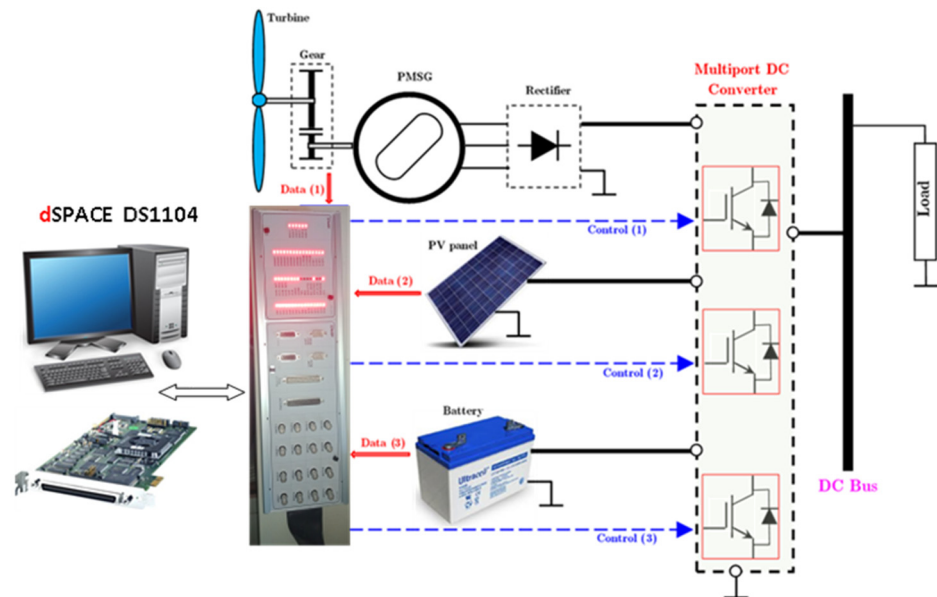


Figure 16. Description of the laboratory setup.

The dSPACE1104 contains two DSPs, a *Motorola MPC8240* processor (*master*) with a PPC 603e core and on-chip peripherals, 250 MHz, and a *Texas Instruments TMS320F240* DSP (*slave*), 20 MHz.

The panel interface of dSPACE1104 is presented in Figure 17. It contains eight Analog Digital Converters (ADC) for input, eight Digital Analog Converters (DAC) for output, one connector PWM (12 pins) and two incremental encoders (that we need).

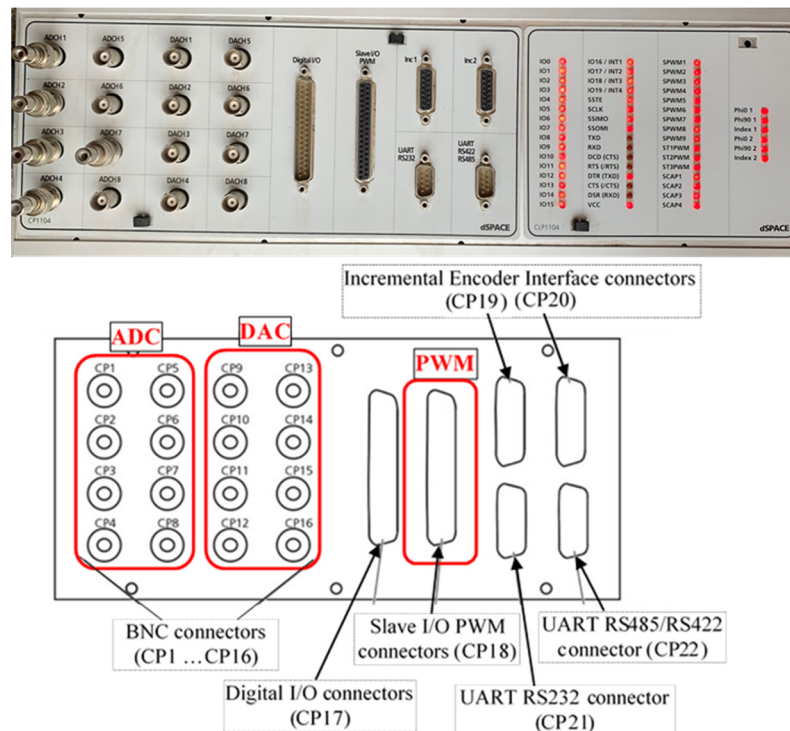


Figure 17. Panel interface of dSPACE1104.

Figure 18 shows the adaptation interface of the 5 V PWM signal generated by the system for the control of the IGBT power module driver with 15 V (case of wind or PV). For the battery in Figure 19, we used two switches, an IGBT power module (half bridge: “bidirectional branch) and two gates to activate the boost mode or buck mode (shown in Figures 11 and 12).

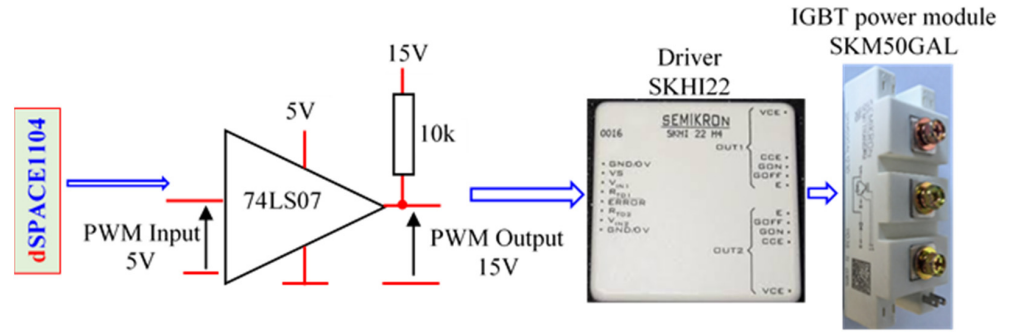


Figure 18. Interface adaptation of the 5 V PWM (for wind and PV).

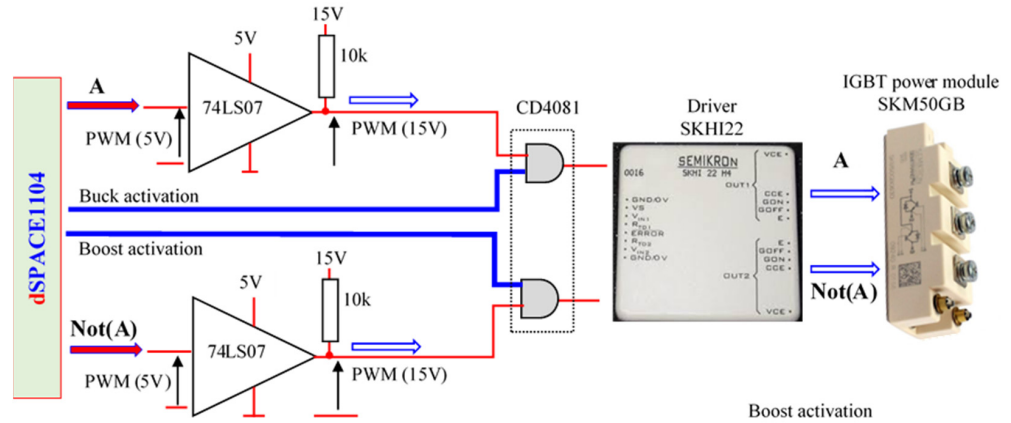


Figure 19. Interface adaptation of the 5 V PWM (for battery).

For activate boost mode and buck mode, a simple method has been proposed as presented in Figure 20. If the current  $I_{3-ref}$  is positive, the boost mode is activated, then the battery is in the discharge phase. However, boost mode is activated if  $I_{3-ref}$  is negative (charge phase), and we note that  $I_{3-ref}$  is set by the voltage controller.

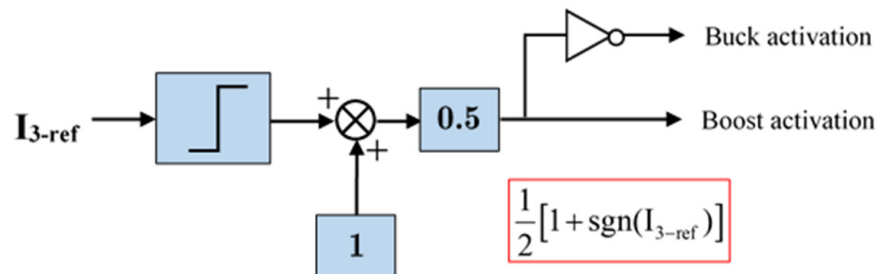


Figure 20. Boost and buck activation mode.

The implementation of the control law is presented in Figure 21 according to the proposed control Equation (19). The controller output is connected to the DS1104SL\_DSP\_PWM3 port.

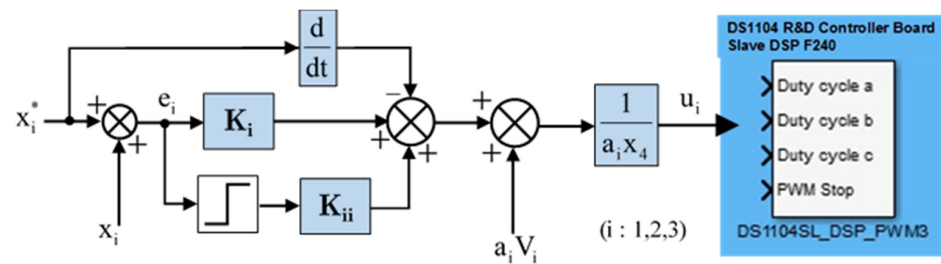


Figure 21. Implementation of the robust control law on dSPACE1104.

4.1. Wind Turbine Emulator

The wind turbine was emulated by using a DC motor of 250 W rated power, controlled through a chopper in external mode (analog 0–10 V) using a speed closed loop as shown in Figure 22.

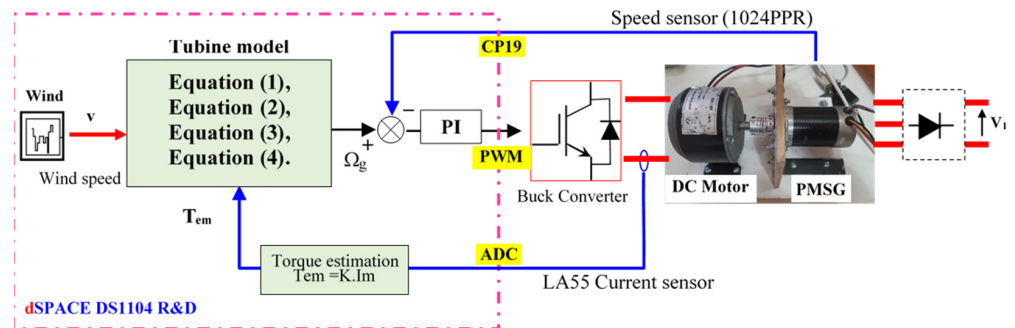


Figure 22. Implementation of the wind turbine emulator.

4.2. Photovoltaic Panel Emulator

The PV was emulated using a linear amplifier (35 V–175 W) rated power, directly controlled by the Digital Analog Converter (DAC) output of dSPACE1104 (analog 0–10 V) and using a current and voltage closed loop as shown in Figure 23. To simplify the implementation of the PV emulator, Equation (8) has been rewritten as (25). Then, the control signal of the linear amplifier was normalized by dividing by  $V_{oc}$  (open-circuit voltage of the panel) and multiplying by 10 (max voltage of the DAC):

$$V_{pv} = \frac{nKT}{e} \cdot \left[ \ln \left( \frac{N_p I_{ph} - I_{pv}}{N_p I_{sat}} \right) + 1 \right] - \left( I_{pv} \frac{N_p}{N_s} R_s \right), \tag{25}$$

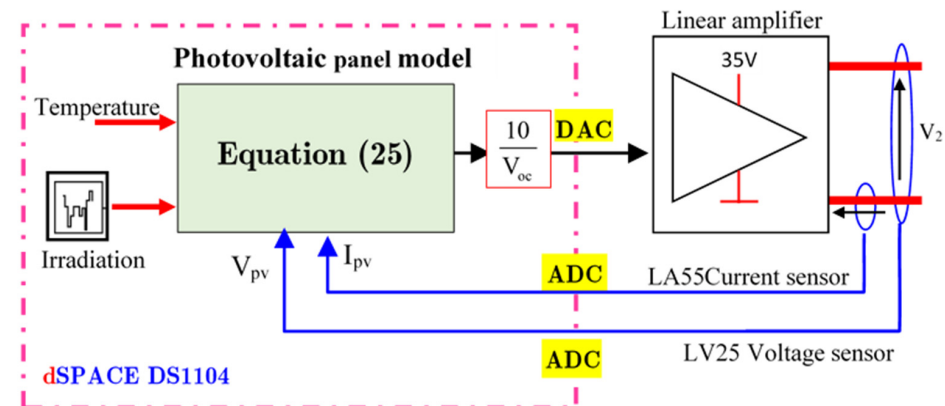


Figure 23. Implementation of the PV emulator.

### 4.3. Profiles

Figure 24 shows the wind, solar irradiation and load applied profiles 1. The wind speed changes from 7.5 m/s to 4 m/s at 8 s, the irradiation changes from 1000 W/m<sup>2</sup> to 500 W/m<sup>2</sup> at 3 s and finally the load changes from 150 Ω to 75 Ω at 13 s. In order to approach the real operating conditions, second wind and irradiation profiles are applied as shown in Figure 25.

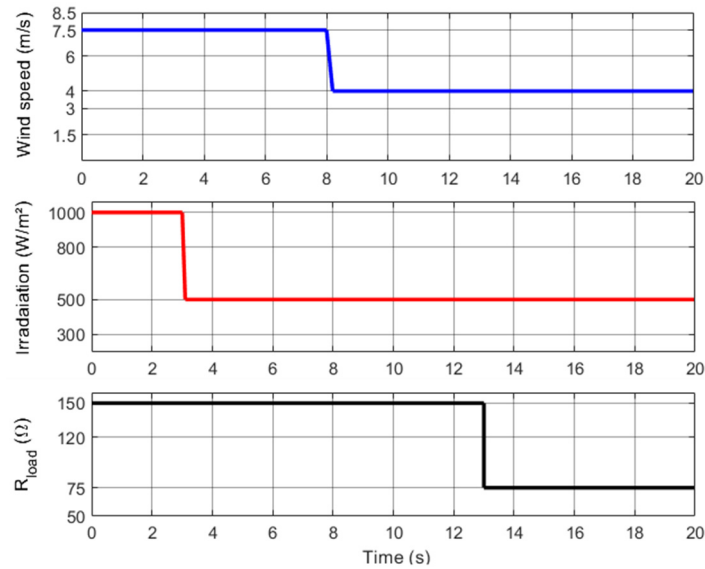


Figure 24. Wind speed and irradiance load profiles 1.

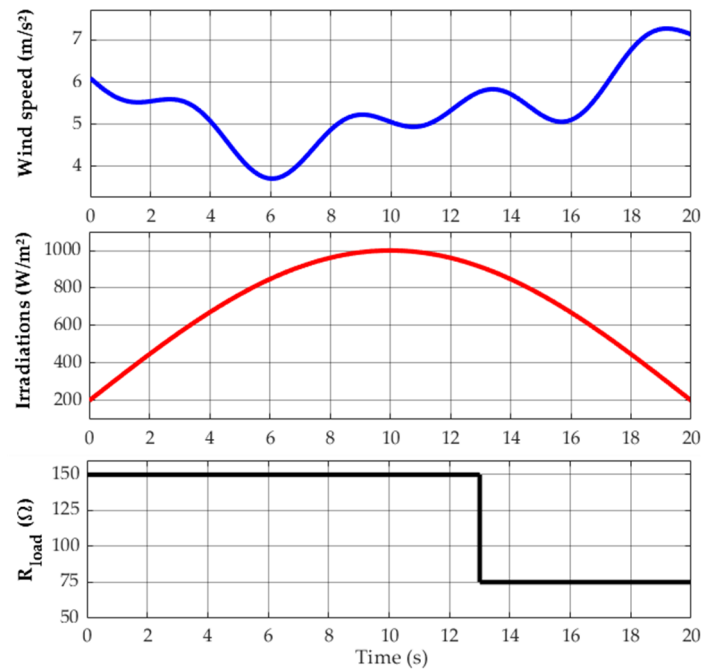


Figure 25. Wind speed and irradiance load profiles 2.

## 5. Experimental Results

Figures 26 and 27 present the current generated by PMSG according to the TSR-MPPT, the current generated PV according to the look-up table MPPT and the battery current and DC-Bus output voltage for the imposed profiles in Figures 24 and 25.

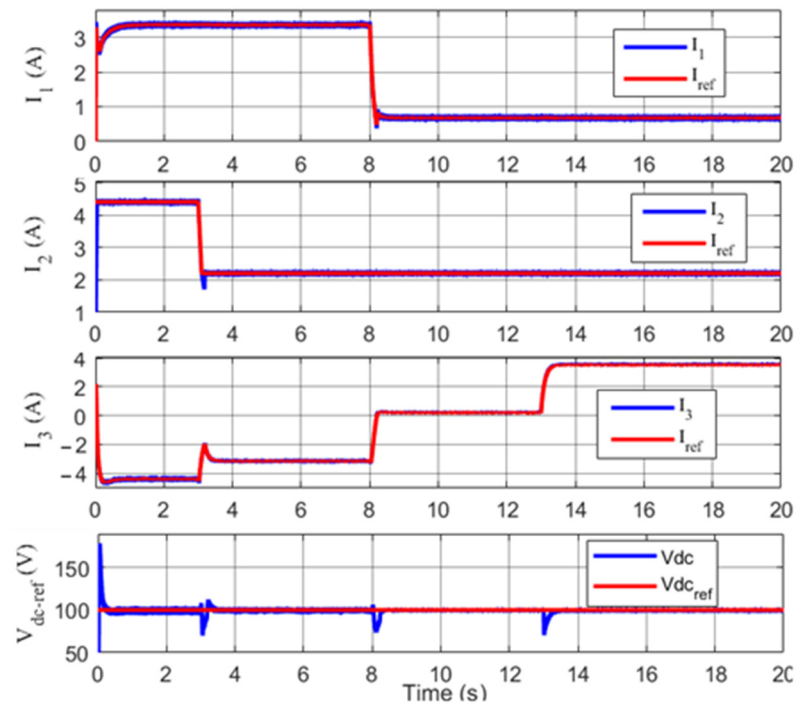


Figure 26. Input currents for control and Vdc voltage results.

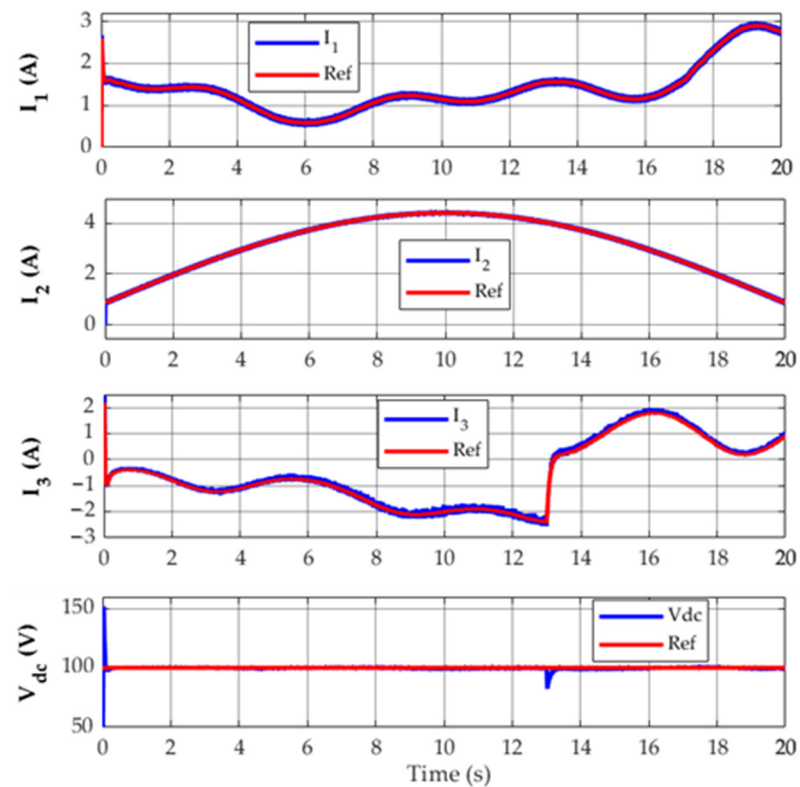


Figure 27. Input currents for control and Vdc voltage results.

Figures 28 and 29 present the speed of the wind turbine and the power coefficient under wind, irradiation and load variations.

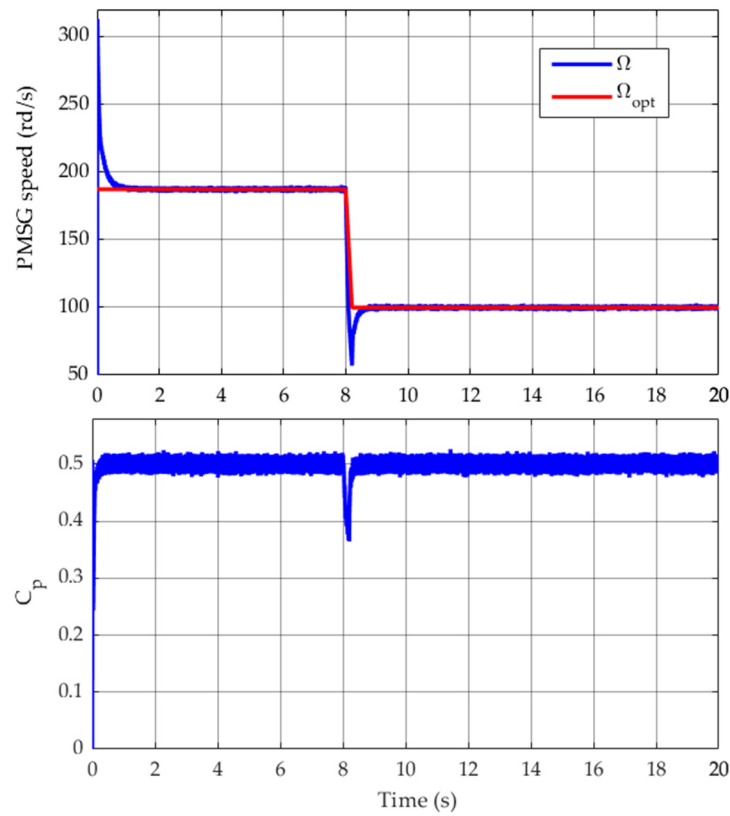


Figure 28. Speed and power coefficient according to wind MPPT.

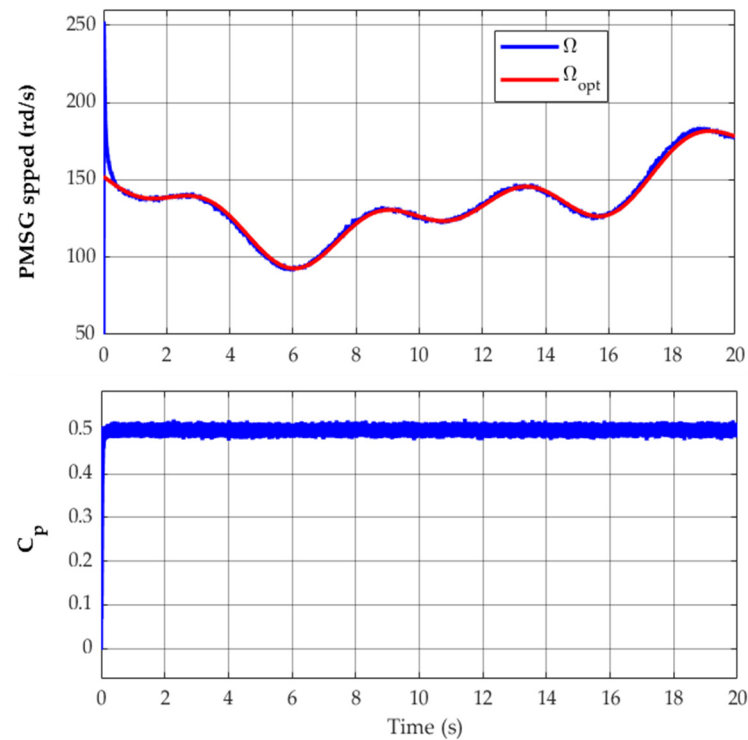


Figure 29. Speed and power coefficient according to wind MPPT.

Figures 30 and 31 present the power of the wind system, the power of the PV system, the power of the battery and the state of charge (SOC) under the variation conditions given in the profiles in Figures 24 and 25.

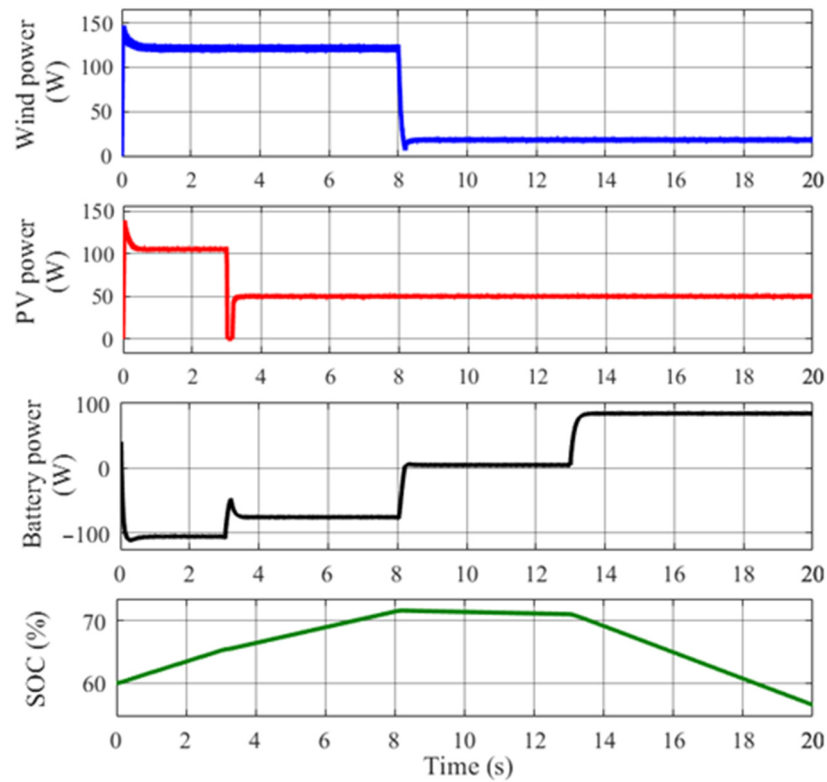


Figure 30. Wind power, PV power, battery power and SOC.

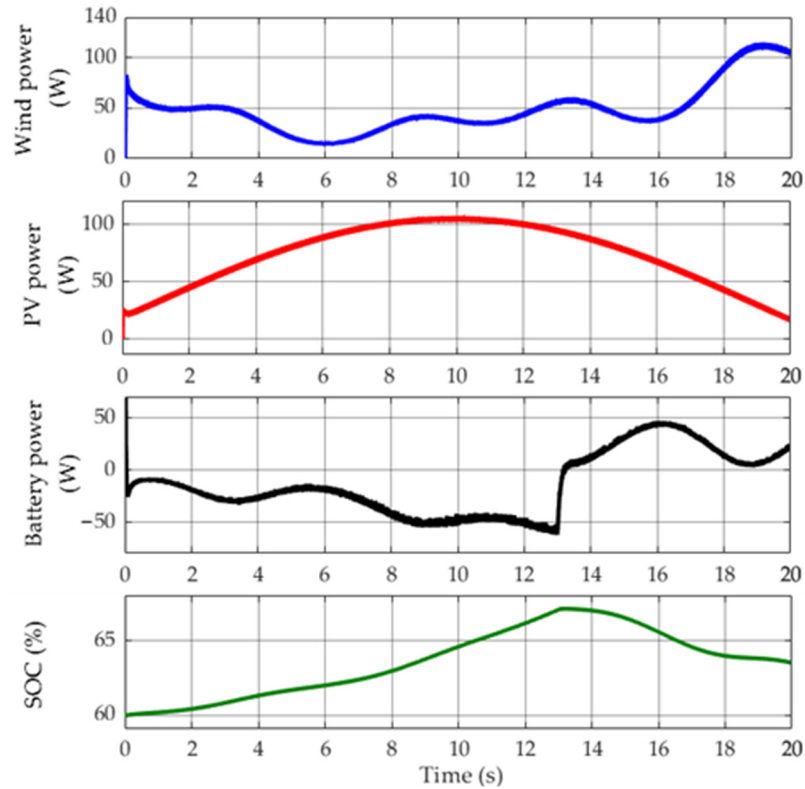


Figure 31. Wind power, PV power, battery power and SOC.

### 6. Discussion

Despite of the change in wind speed, irradiation and load, the results show that PV current, PMSG current, battery current, DC-Bus voltage and the speed turbine reach

their references rapidly, Figures 26 and 27. In spite of the wind speed change, the power coefficient remained constant with maximal value (0.515). The turbine speed reached its optimal value, so it takes the same profile as the wind speed, although it still tracks its reference. The results confirm the good tracking of the proposed control and the system operates in optimal conditions even under wind, irradiation and load variations (Figures 28 and 29).

The DC-Bus voltage tracks its reference thanks to the battery because it stores the excess energy and restores it if there is an energy deficit; see Figures 30 and 31. The battery absorbs the excess power and ensures the power balance of the wind and PV hybrid system. Even if the system operates at variable conditions (wind speed, irradiations, load), the DC-Bus voltage remains stable, as shown in Figures 26 and 27. This result confirms the robustness of the proposed control method. Figures 30 and 31 illustrate the power flow of each system component (solar, wind, battery and load profile).

For  $t < 13$  s, the load is mainly powered by the hybrid system (PV-Wind) and the available power is greater than the power demand of the load. We notice that the battery power is negative, which signified the charging of the battery. After 13 s, the available hybrid power (PV-Wind) is less than the load power. The battery power becomes positive, which means the battery discharges.

This effect can also be observed in the battery state of charge (SOC). The battery guarantees the stability and energy balance of the system. Additionally, it can be seen from the figure that the total SOC is proportional to the battery power as shown in the figure. In case there is a surplus of energy, the system charges the battery with the energy generated from photovoltaic energy and wind turbines, where the SOC value increases. In the case of a lack of power for the loads, the battery performs a discharge, and the SOC value decreases.

We can confirm that the control is robust and ensures the good tracking of all currents to their reference under parameter variations; Figures 26 and 27. The results prove the effectiveness of the proposed control.

## 7. Conclusions

In this work, a robust current control for hybrid PV-wind systems is proposed with the objective of providing continuous power to a load.

The nonlinear robust control structure is based on Lyapunov theory to control a hybrid PV-Wind system and the designed current controller surpasses the system nonlinear model and improves robustness. The proposed control guarantees asymptotic stability.

Additionally, a multiport DC converter has been proposed as an effective solution compared to conventional converter topology for integrating two renewable energy sources with different voltage levels, such as solar and wind.

We have found that the topology proposed in this paper has proven to be efficient and optimal from the control point of view because it allows us to stabilize the DC-Bus voltage and optimizes the number of power components with a minimum of PWM controllers. Additionally, it allows a balance of energy in the system and decreases the speed, voltage and current oscillations.

The overall system has been validated on an experimental test bench and implemented on the DSP1104. The results show that the proposed control improved the system's stability, as well as the feasibility and validity of the proposed scheme.

**Author Contributions:** Conceptualization, F.M., S.D., L.C.-A. and N.N.-S.; methodology, S.D.; software, F.M. and S.D.; validation, F.M., S.D., L.C.-A. and N.N.-S.; formal analysis, S.D. and L.C.-A.; investigation, F.M. and S.D.; resources, F.M.; data curation, S.D.; writing—original draft preparation, F.M.; writing—review and editing, S.D., L.C.-A. and N.N.-S.; visualization, L.C.-A.; supervision, S.D.; project administration, S.D.; funding acquisition, not available. All authors have read and agreed to the published version of the manuscript.

**Funding:** This research received no external funding.

**Institutional Review Board Statement:** Not applicable.

**Informed Consent Statement:** Not applicable.

**Data Availability Statement:** Not applicable.

**Conflicts of Interest:** The authors declare no conflict of interest.

## Nomenclature

The following abbreviations are used in this manuscript:

HRES	Hybrid renewable energy system
PV	Photovoltaic
RES	Renewable energy system
DC	Direct current
AC	Alternating current
RES	Renewable energy system
MP	Multiport
MPC	Multiport converters
PV	Photovoltaic
WBG	Wide bandgap
$C_p$	Power coefficient
PMSG	Permanent magnet synchronous generator
MPPT	Maximum power point tracking
PWM	Pulse width modulation
IGBT	Insulated-gate bipolar transistor
T	Transistor
D	Diode
SOC	State of charge
$P_T$	Turbine Aerodynamic power
A	The area swept by the rotor blades
v	Wind speed
$\beta$	Pitch angle
$\lambda$	Tip-Speed Ratio (TSR)
$\omega$	Rotor electric speed
$\Omega$	Mechanical speed
$R_s$	Stator resistance of PMSG
$I_d$	Stator direct current of PMSG
$I_q$	Stator quadrature current of PMSG
$V_d$	Stator direct voltage of PMSG
$V_q$	Stator quadrature voltage of PMSG
$L_d$	Stator direct inductance of PMSG
$L_q$	Stator quadrature inductance of PMSG
$\phi_f$	Flux of the permanent magnet.
$I_{sat}$	Reverse saturation current
K	Boltzmann's constant
T	Temperature
e	electron charge
n	Ideality factor
$I_{ph}$	Photonic current
$V_{pv}$	PV voltage
$I_{pv}$	PV current
$N_p$	Parallel cells
$N_s$	Series cells
$I_{sc}$	Storage current
$I_{wc}$	Output wind current
$I_{pvc}$	Output PV current
$I_{rew}$	Renewable current

## References

1. Praveen Kumar, T.; Subrahmanyam, N.; Sydulu, M. Power flow management of the grid-connected hybrid renewable energy system: A PLSANN control approach. *IETE J. Res.* **2021**, *67*, 569–584. [\[CrossRef\]](#)
2. Nazari, M.A.; Rungamornrat, J.; Prokop, L.; Blazek, V.; Misak, S.; Al-Bahrani, M.; Ahmadi, M.H. An updated review on integration of solar photovoltaic modules and heat pumps towards decarbonization of buildings. *Energy Sustain. Dev.* **2023**, *72*, 230–242. [\[CrossRef\]](#)
3. Tagayi, R.K.; Han, S.; Lee, H.; Kim, J. Reliable Frequency Control Support Scheme Based on Wind Power Generator Combined with Rechargeable Energy Storage System Applying Adaptive Power Reference. *Appl. Sci.* **2023**, *13*, 5302. [\[CrossRef\]](#)
4. Alayi, R.; Seydnouri, S.R.; Jahangeri, M.; Maarif, A. Optimization, sensitivity analysis, and techno-economic evaluation of a multi-source system for an urban community: A case study. *Renew. Energy Res. Appl.* **2022**, *3*, 21–30.
5. Fatah, A.; Benlaloui, I.; Mechnane, F.; Boutabba, T.; Khamari, D.; Drid, S.; Chrifi-Alaoui, L. A Modified Perturbe and Observe MPPT Technique for Standalone Hybrid PV-Wind with Power Management. In Proceedings of the International Conference on Control, Automation and Diagnosis (ICCAD), Grenoble, France, 3–5 November 2021.
6. Elbaset, A.A.; Ali, H.; Abd-El Sattar, M.; Khaled, M. Implementation of a modified perturb and observe maximum power point tracking algorithm for photovoltaic system using an embedded microcontroller. *IET Renew. Power Gener.* **2016**, *10*, 551–560. [\[CrossRef\]](#)
7. Feng, S.; Wang, K.; Lei, J.; Tang, Y. Influences of DC bus voltage dynamics in modulation algorithm on power oscillations in PMSG-based wind farms. *Int. J. Electr. Power Energy Syst.* **2021**, *124*, 106387. [\[CrossRef\]](#)
8. Deshmukh, R.; Phadke, A.; Callaway, D. Least-cost targets and avoided fossil fuel capacity in India's pursuit of renewable energy. *Proc. Natl. Acad. Sci. USA* **2021**, *118*, e2008128118. [\[CrossRef\]](#)
9. Akbari, E.; Sheikholeslami, A.R.; Zishan, F. Participation of Renewable Energy in Providing Demand Response in Presence of Energy Storage. *Renew. Energy Res. Appl.* **2023**, *4*, 225–234.
10. Maleki, A.; Nazari, M.A.; Pourfayaz, F. Harmony search optimization for optimum sizing of hybrid solar schemes based on battery storage unit. *Energy Rep.* **2020**, *6*, 102–111. [\[CrossRef\]](#)
11. Kadam, A.H.; Menon, R.; Williamson, S.S. A novel bidirectional three-phase ac-dc/dc-ac converter for pmsm virtual machine system with common dc bus. In Proceedings of the IEEE Applied Power Electronics Conference and Exposition (APEC), San Antonio, TX, USA, 4–8 March 2018; pp. 1944–1951.
12. Naik, M.V.; Samuel, P. Analysis of ripple current, power losses and high efficiency of DC–DC converters for fuel cell power generating systems. *Renew. Sustain. Energy Rev.* **2016**, *59*, 1080–1088. [\[CrossRef\]](#)
13. Mahjoub, S.; Ayadi, M.; Derbel, N. Comparative study of smart energy management control strategies for hybrid renewable system based Dual Input-Single Output DC-DC Converter. *J. Electr. Syst.* **2020**, *16*, 218–234.
14. Mumtaz, F.; Yahaya, N.Z.; Meraj, S.T.; Singh, B.; Kannan, R.; Ibrahim, O. Review on non-isolated DC-DC converters and their control techniques for renewable energy applications. *Ain Shams Eng. J.* **2021**, *12*, 3747–3763. [\[CrossRef\]](#)
15. Asghari Gorji, S.; Sahebi, H.G.; Ektesabi, M.M.; Rad, A.B. Topologies and control schemes of bidirectional DC–DC power converters: An overview. *IEEE Access* **2019**, *7*, 117997–118019. [\[CrossRef\]](#)
16. Hadmer, B.; Drid, S.; Kouzou, A.; Mechnane, F.; Chrifi-Alaoui, L.; Drid, M.D. SPWM and Third Harmonique Injection Techniques for 7-Level Packed U-Cell Inverter. In Proceedings of the IEEE 21st international Ccnference on Sciences and Techniques of Automatic Control and Computer Engineering (STA), Sousse, Tunisia, 19–21 December 2022; pp. 508–511.
17. Aderinto, T.; Li, H. Review on power performance and efficiency of wave energy converters. *Energies* **2019**, *12*, 4329. [\[CrossRef\]](#)
18. Kish, G.J. On the emerging class of non-isolated modular multilevel DC–DC converters for DC and hybrid AC–DC systems. *IEEE Trans. Smart Grid* **2017**, *10*, 1762–1771. [\[CrossRef\]](#)
19. Ye, Y.-M.; Cheng, K.W.E. Multi-input voltage-summation converter based on switched-capacitor. *IET Power Electron.* **2013**, *6*, 1909–1916.
20. Mechnane, F.; Drid, S.; Hadmer, B.; Nait-Said, N.; Chrifi-Alaoui, L.; Delahoche, L. Robust Control of a PV-Wind Hybrid System Using DISO DC/DC Converter. In Proceedings of the 19th International Multi-Conference on Systems, Signals & Devices (SSD), Sétif, Algeria, 6–10 May 2022; pp. 1788–1794.
21. Mahjoub, S.; Labdai, S.; Chrifi-Alaoui, L.; Drid, S.; Derbel, N. Design and implementation of a Fuzzy logic supervisory based on SMC controller for a Dual Input-Single Output converter. *Int. J. Electr. Power Energy Syst.* **2023**, *150*, 109053. [\[CrossRef\]](#)
22. Babaei, E.; Abbasi, O. Structure for multi-input multi-output dc–dc boost converter. *IET Power Electron.* **2016**, *9*, 9–19. [\[CrossRef\]](#)
23. Krishnamurthy, K.; Padmanaban, S.; Blaabjerg, F.; Neelakandan, R.B.; Prabhu, K.R. Power electronic converter configurations integration with hybrid energy sources—a comprehensive review for state-of-the-art in research. *Electr. Power Compon. Syst.* **2019**, *47*, 1623–1650. [\[CrossRef\]](#)
24. Rehman, Z.; Al-Bahadly, I.; Mukhopadhyay, S. Multiinput DC–DC converters in renewable energy applications—An overview. *Renew. Sustain. Energy Rev.* **2015**, *41*, 521–539. [\[CrossRef\]](#)
25. Gevorkov, L.; Domínguez-García, J.L.; Romero, L.T.; Martínez, À.F. Modern MultiPort Converter Technologies: A Systematic Review. *Appl. Sci.* **2023**, *13*, 2579. [\[CrossRef\]](#)
26. Litrán, S.P.; Durán, E.; Semião, J.; Díaz-Martín, C. Multiple-Output DC–DC Converters: Applications and Solutions. *Electronics* **2022**, *11*, 1258. [\[CrossRef\]](#)

27. Fong, Y.C.; Cheng, K.W.E.; Raman, S.R.; Wang, X. Multi-Port Zero-Current Switching Switched-Capacitor Converters for Battery Management Applications. *Energies* **2018**, *11*, 1934. [[CrossRef](#)]
28. Yalla, S.P.; Subudhi, P.S.; Ramachandaramurthy, V.K. Topological review of hybrid RES based multi-port converters. *IET Renew. Power Gener.* **2022**, *16*, 1087–1106. [[CrossRef](#)]
29. Huang, Z.; Zhou, D.; Wang, L.; Shen, Z.; Li, Y. A Review of Single-Stage Multiport Inverters for Multisource Applications. *IEEE Trans. Power Electron.* **2023**, *38*, 6566–6584. [[CrossRef](#)]
30. Jeong, Y.S.; Lee, S.H.; Jeong, S.G.; Kwon, J.M.; Kwon, B.H. High-efficiency bidirectional grid-tied converter using single power conversion with high-quality grid current. *IEEE Trans. Ind. Electron.* **2017**, *64*, 8504–8513. [[CrossRef](#)]
31. Nguyen, M.K.; Duong, T.D.; Lim, Y.C.; Kim, Y.J. Isolated boost DC–DC converter with three switches. *IEEE Trans. Power Electron.* **2017**, *33*, 1389–1398. [[CrossRef](#)]
32. Aghdam, B.A.; Nia, P.H.; Nazarpour, D. A new multi-port DC/DC converter for PV/battery/DC grid energy systems. In Proceedings of the 9th Iranian Conference on Renewable Energy & Distributed Generation (ICREDG), Mashhad, Iran, 23–24 February 2022.
33. Shi, H.; Sun, K.; Wu, H.; Li, Y.; Xiao, X. Unified state-space modeling method for dual-active-bridge converters considering bidirectional phase shift. In Proceedings of the IEEE Energy Conversion Congress and Exposition (ECCE), Portland, OR, USA, 23–27 September 2018; pp. 643–649.
34. Zeng, J.; Qiao, W.; Qu, L.; Jiao, Y. An isolated multiport DC–DC converter for simultaneous power management of multiple different renewable energy sources. *IEEE J. Emerg. Sel. Top. Power Electron.* **2013**, *2*, 70–78. [[CrossRef](#)]
35. Baek, S.; Bhattacharya, S. Analytical modeling and implementation of a coaxially wound transformer with integrated filter inductance for isolated soft-switching DC–DC converters. *IEEE Trans. Ind. Electron.* **2017**, *65*, 2245–2255. [[CrossRef](#)]
36. Zhang, Z.; Pittini, R.; Andersen, M.A.; Thomsena, O.C. A review and design of power electronics converters for fuel cell hybrid system applications. *Energy Procedia* **2012**, *20*, 301–310. [[CrossRef](#)]
37. Farjah, E.; Rezaee, S.; Ghanbari, T. Sliding mode control of a novel multi-input split-inductor buck-boost converter. In Proceedings of the 25th IEEE Canadian Conference on Electrical and Computer Engineering (CCECE), Montreal, QC, Canada, 29 April–2 May 2012.
38. Deshmukh, N.B.; Thombare, R.D.; Jadhav, P.T.; More, D.S. MISO Luo DC-DC converter for renewable energy applications. In Proceedings of the International Conference on Energy Systems and Applications, Pune, India, 30 October–1 November 2015; pp. 63–68.
39. Irmak, E.; Güler, N. Application of a boost based multi-input single-output DC/DC converter. In Proceedings of the IEEE 6th International Conference on Renewable Energy Research and Applications (ICRERA), San Diego, CA, USA, 5–8 November 2017; pp. 955–961.
40. Bossoufi, B.; Karim, M.; Lagrioui, A.; Taoussi, M.; Derouich, A. Observer backstepping control of DFIG-Generators for wind turbines variable-speed: FPGA-based implementation. *Renew. Energy* **2015**, *81*, 903–917. [[CrossRef](#)]
41. Villalva, M.G.; Gazoli, J.R.; Ruppert Filho, E. Comprehensive approach to modeling and simulation of photovoltaic arrays. *IEEE Trans. Power Electron.* **2009**, *24*, 1198–1208. [[CrossRef](#)]
42. Mechnane, F.; Drid, S.; Sahraoui, H.; Benlaloui, I.; Boutabba, T.; Nait-Said, N.; Chrifi-Alaoui, L. Implementation of Super-twisting control with Photovoltaic System Emulator. In Proceedings of the International Conference on Control, Automation and Diagnosis (ICCAD), Grenoble, France, 3–5 November 2021.
43. Khalil, H. *Nonlinear Systems*, 2nd ed.; Prentice-Hall: Englewood Cliffs, NJ, USA, 1996.

**Disclaimer/Publisher’s Note:** The statements, opinions and data contained in all publications are solely those of the individual author(s) and contributor(s) and not of MDPI and/or the editor(s). MDPI and/or the editor(s) disclaim responsibility for any injury to people or property resulting from any ideas, methods, instructions or products referred to in the content.